**Ed Habtour**[1]
Department of Aerodynamics and Astronautics,
The University of Washington,
Seattle, WA 98195
e-mail: habtour@uw.edu

**Dario Di Maio**
Department of Mechanical Engineering,
University of Twente,
Enschede 7522 NB, The Netherlands

**Thijs Masmeijer**
Department of Mechanical Engineering,
University of Twente,
Enschede 7522 NB, The Netherlands

**Laura Cordova Gonzalez**
Department of Industrial and Materials Science,
Chalmers University of Technology,
Gothenburg, Sweden

**Tiedo Tinga**
Department of Mechanical Engineering,
University of Twente,
Enschede 7522 NB, The Netherlands;
The Netherlands Defence Academy,
Den Helder,
The Netherlands

# Highly Sensitive Nonlinear Identification to Track Early Fatigue Signs in Flexible Structures

*This study describes a physics-based and data-driven nonlinear system identification (NSI) approach for detecting early fatigue damage due to vibratory loads. The approach also allows for tracking the evolution of damage in real-time. Nonlinear parameters such as geometric stiffness, cubic damping, and phase angle shift can be estimated as a function of fatigue cycles, which are demonstrated experimentally using flexible aluminum 7075-T6 structures exposed to vibration. NSI is utilized to create and update nonlinear frequency response functions, backbone curves and phase traces to visualize and estimate the structural health. Findings show that the dynamic phase is more sensitive to the evolution of early fatigue damage than nonlinear parameters such as the geometric stiffness and cubic damping parameters. A modified Carrella–Ewins method is introduced to calculate the backbone from nonlinear signal response, which is in good agreement with the numerical and harmonic balance results. The phase tracing method is presented, which appears to detect damage after approximately 40% of fatigue life, while the geometric stiffness and cubic damping parameters are capable of detecting fatigue damage after approximately 50% of the life-cycle.* [DOI: 10.1115/1.4052420]

*Keywords: system identification, high-order, diagnostics, signal processing, early fatigue, detection, nonlinear dynamics, phase tracing*

## 1 Introduction

It is quite remarkable to witness just in the past decade the technological achievements made to improve fuel efficiency, speed and travel range in modern aerospace and automotive vehicles, and robots. Some of the key enablers of these achievements are recent advancements in light-weight materials [1], morphing structures [2], structural optimization [3], and fluid–solid interaction modeling [4]. While those achievements have been pivotal in generating a new class of advanced structures optimized for performance, these modern structures are becoming highly flexible and thus susceptible to vibration, shock, or impact damage [5]. Consequently, three major engineering challenges have emerged from light structure designs: (i) amplification of dynamic nonlinearities due to high elastic deformation [6]; (ii) limited physics-based identification tools for connecting nonlinearities due to local material degradation to collective global dynamics [7]; thus (iii) detecting early fatigue damage via current diagnostics and health monitoring systems is often formidable. To ameliorate those challenges, significant structural health diagnostic, prognostic, and monitoring technologies are beginning to leverage new advancements in system identification (SI) tools for improving detection sensitivity to early signs of fatigue damage [8,9]. In fact, structural health monitoring [10] and prognostics and health management [11] utilize a variety of SI algorithms for identifying and tracking changes in the baseline structural dynamic features intrinsic to the component of interest. When using SI for damage detection and health monitoring systems, the main objective is to relate anomalies in the baseline structural dynamic features to early signs of damage before reaching a critical failure [12], thus ensuring the safety and extending the service life of high-value engineering systems.

In this section, a brief background on linear and nonlinear system identification (NSI) is provided in Sec. 1.1 with focus on damage detection and monitoring. For completeness, some of the latest NSI approaches for improving detection sensitivity to early fatigue damage are highlighted in Sec. 1.2. The proposed physics-based NSI approach is described in Sec. 1.3. Sections 2 and 3 detail the analytical development and experimental approach for the proposed fatigue detection approach, respectively. The results and findings of this study are reported and discussed in Sec. 4.

**1.1 Linear and Nonlinear System Identification.** SI can be defined as an engineering process for modeling dynamic systems mostly based on their input and output signals [13,14]. In aerospace, automotive and robotic applications and structures are often exposed to harsh dynamic environments [15]. Such structures can be thought of as systems with their own intrinsic dynamic parameters. When an excitation is applied to a structure, it is recorded as an input signal and its resulting dynamics as an output signal. The dynamic parameters are then extracted from the structural features embedded in the system output signals. Any changes in the parameters from the established baseline dynamics of the system are leveraged to identify potential damage or failures [16,17]. The estimated dynamic parameters from an output signal can be utilized for detecting instabilities [18], faults [19], or disturbances in the system components [20], and subsequently for estimating their impact on the overall performance [21,22].

In general, the distinction between linear and nonlinear systems can be made by examining how the output signals are mapped mathematically to the inputs. A system is considered to be linear when it obeys the principle of superposition:

$$f(ax + by) = af(x) + bf(y) \tag{1}$$

[1]Corresponding author.

Manuscript received April 28, 2021; final manuscript received August 29, 2021; published online October 13, 2021. Assoc. Editor: Wieslaw Ostachowicz.

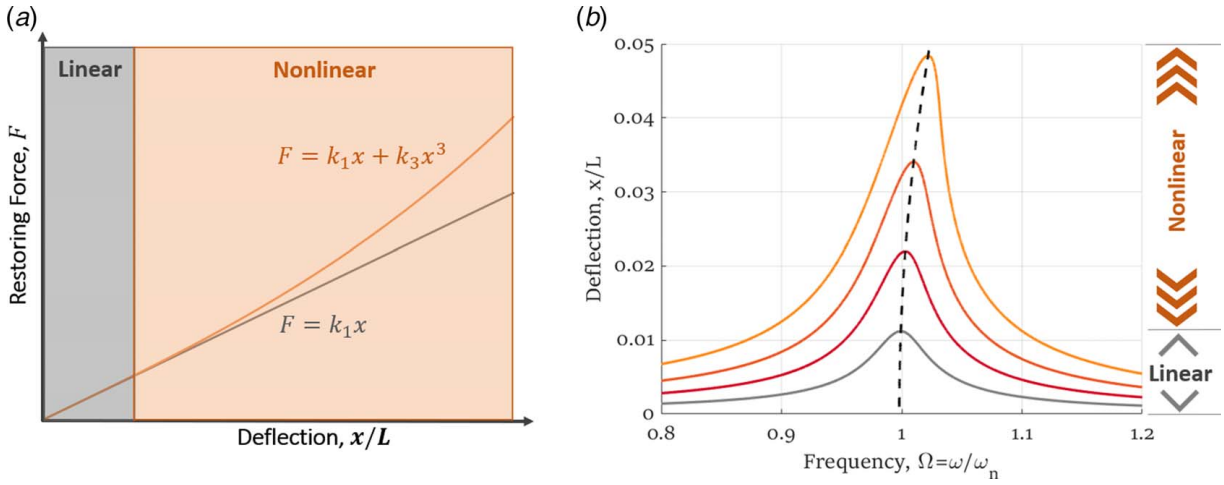


**Fig. 1 (*a*) Restoring force for linear and nonlinear elastic deflections and (*b*) frequency response near the structural resonance transition from linear (in gray) to nonlinear regime (in red to orange) due to high amplitude excitation. The dotted curve is the backbone.**

where $a$ and $b$ are constants, and $x$ and $y$ are input signals. The superposition principle implies that the additive and homogeneity conditions are satisfied, otherwise, the system is considered to be nonlinear [23]. In general, Hooke's law is a good approximation for structures exhibiting linear elastic response due to the application of external loads in the form of restoring forces proportional to the structural displacement, $x$, as shown in Fig. 1(*a*). Flexible structures can endure large reversible deformations before their inherent stress–strain characteristics show any significant departure from their linear regime. In fact, kinematic nonlinearity generates dynamic hardening at the first flextural mode, as shown in Fig. 1(*b*), which is a restoring force proportional to the cubic structural displacement, $x^3$ [24]. For a beam element, flextural displacement >1.0% than the beam length is considered nonlinear. The total restoring force becomes a function of the linear structural stiffness, $k_1$, and nonlinear geometric stiffness, $k_3$, as follows:

$$F(x) = (k_1 + k_3x^2)x \tag{2}$$

One of the early SI techniques applied for detecting damage is linear dynamic parameters extraction, also referred to as modal analysis [25]. This technique provides insights into dynamic features such as vibration modes [26], internal resonances [27], damping [28], and structural stiffness [21]. Modal analysis can be employed to relate fatigue life to the dynamic parameters of structures subjected to shock [29], harmonic [30], rotational [24], or random excitation [31]. When conducting modal analysis, the effect of nonlinearities are often neglected, due to the assumption of invariant dynamic parameters [32]. However, modal analysis cannot accurately describe the dynamic behaviors of most engineering systems since the parameters are dependent on the magnitude of the applied excitation [33,34]. In reality, most engineering structures exhibit various nonlinear behaviors [35,36]. Engineers are often confronted with geometric and damping nonlinearities in a variety of systems with flexible structural components such as aircraft wings [37], blades [38], composite structures [29,39], electronics [40], robots [41], and micro devices [42,43].

Through NSI, the detection sensitivity to microscopic damage features can be amplified by extracting the nonlinear parameters from the outputs such as geometric stiffness and gyroscopic inertia [32]. Changes in the nonlinear geometric stiffness were related experimentally to material fatigue precursors such as the occurrence of microplasticity [44,45], crystal reorientation [46], and microscopic cracks [3] using techniques such as atomic force microscopy [47], Eddy current [48], and ultrasound [49]. The backbone curves can be leveraged to track the softening or hardening behaviors due to the development of fatigue crack, Fig. 1(*b*).

**1.2 System Identification Tools.** It is important to highlight commonly used methods to overcome challenges related to the computational requirement for solving nonlinear dynamic models and high signal-to-noise ratio demand for data processing [20]. The equations of motion can be solved algebraically using techniques such as the harmonic balance method (HBM) [50], incremental HBM [51], method of averaging [52], Volterra series [53], normal form [54], nonlinear normal modes [55], or multiple scales [56,57]. In this study, HBM was applied to analytically solve the equation of motion, where the results were in good agreement with the numerical solution. From a data processing perspective, methods for extracting nonlinear dynamic features are, but not limited to, adaptive and deep learning [58–60], data and deep fusion [13,61], cascaded optimization [62], neural networks [63], multi-agent-based modeling [64], and Bayesian dynamic network [65]. Various filtering techniques such as modified Kalman and adaptive particle filters were utilized successfully to improve fatigue predictions [65,66]. The Hilbert transform and wavelet transforms [67–69], and zero-crossing [70] were leveraged for constructing the backbone curves and estimating nonlinear damping coefficient.

**1.3 Physics-Based System Identification Approach.** Our proposed physics-based and data-driven NSI approach for detecting and tracking early signs of fatigue is summarized in Fig. 2. The linear and nonlinear identification processes are shown in gray and orange colors, respectively. The fatigue step, which includes real-time phase and resonance shifts, is displayed in blue (Fig. 2). This approach was demonstrated experimentally and analytically using beam-like structures fabricated from aluminum 7075-T6 aerospace-grade alloy, which was exposed to vibration fatigue. Prior to performing the fatigue test, the baseline linear and nonlinear dynamic features must be established first for each pristine specimen (Fig. 2). The system identification consists of three major steps: (i) identifying the damping coefficients from free vibration, (ii) extracting the stiffness coefficients from slow sine-sweep, and (iii) in situ tracing of the response phase and resonance shifts during vibration fatigue. Free-vibration tests are utilized to calculate the viscous and cubic damping coefficients, $c_1$ and $c_3$, respectively, from the time decay signal [71]. Low and high amplitude slow sine-sweeps are leveraged to extract $k_1$ and $k_3$, the linear and nonlinear stiffness coefficients, respectively [72]. For both free-vibration and sine-sweep steps, linear and nonlinear behaviors are defined as tip displacements <1% and >2% of the total beam length, respectively (Fig. 1). The identification steps are repeated after completing each specified number of fatigue cycles (Fig. 2). In this study, the fatigue life was divided into four 25% segments, approximately $3 \times 10^5$ cycles per segment. The test was terminated

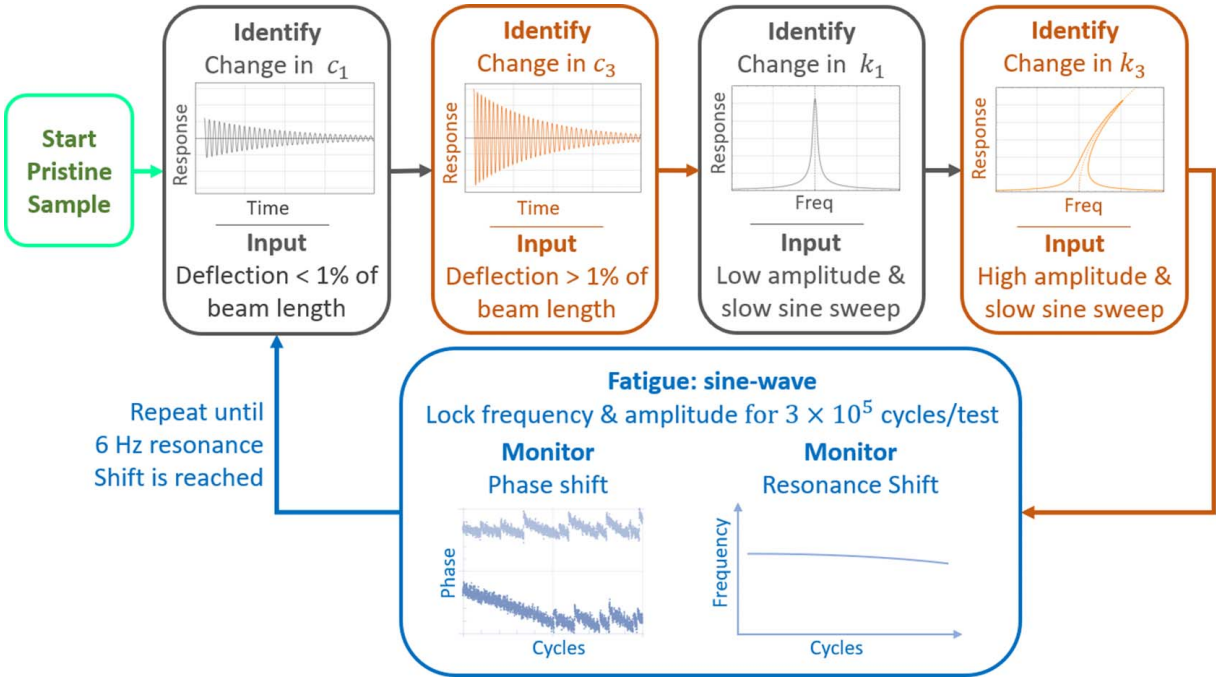


**Fig. 2 Physics-based and data-driven NSI approach for detecting early sign of fatigue damage and tracking its evolution**

when the total resonance shift reached 6 Hz. Details are provided in Sec. 3.

In this study, the sensitivity of each dynamic feature to vibration fatigue was examined as a function of structures' life-cycle. The phase tracing appeared to be the most sensitive feature to early fatigue damage followed by the nonlinear stiffness and damping features. Early fatigue damage is defined as a structure having a remaining useful life >50%. Changes in the linear dynamic features due to structural degradation were insignificant before exhausting 50% of the remaining useful life.

## 2 Mathematical Development

The development of the analytical model for approximating the displacement response of flexible cantilevered beams due to vibration fatigue is detailed in this section. Each beam has a uniform cross-sectional area, $A$, with width $b$ and thickness $h$ along its entire length $L$, as shown in Fig. 3. The beam distributive mass and the rotary inertia are $m_s$ and $I_r$, respectively. The beam is clamped to a rigid support boundary. The vibratory loads are applied to the rigid support in the transverse direction using harmonic excitation with an amplitude $Y$, as shown in Fig. 3.

The beam displacement is approximated using nonlinear Euler–Bernoulli theory since $L/h$ is $\geq 10$ [24]. It is also reasonable to assume that the beam first mode undergoes purely planar flextural vibrations since the structure length to width ratio is $\leq 10$ [44]. Therefore, the effects of torsion and shear deformation can be ignored.

Two coordinate systems are used to describe the deformed and undeformed geometries of the beam. The global Cartesian system describing the undeformed geometry is $xy$. The local $\xi\eta$ orthogonal curvilinear coordinates capture the nonlinear elastic deformation (Fig. 3). Each differential beam element has infinitesimal thickness $ds$. Exciting the rigid support causes each point on the undeformed cross section of the beam to experience an elastic displacement. The deformation with respect to the $x$ and $y$ axes along the beam's undeformed arclength from the fixed-end to a reference point, $s$, at time, $t$, are expressed in terms of a rotational angle, as well as the axial and transverse displacements, $\theta(s, t)$, $u(s, t)$, and $v(s, t)$, respectively. The displacement vector can be expressed as

$$\mathbf{R} = (s + u - \eta \sin\theta)\mathbf{i_x} + (v + \eta \cos\theta)\mathbf{i_y} \tag{3}$$

Substituting the time derivative of $\mathbf{R}$ into the kinetic energy, $T$, yields the following [24]:

$$T = \frac{1}{2}\int_0^L \left[ m_s\left[\dot{u}^2 + \left(\dot{v} + \dot{Y}\right)^2\right] + I_r\dot{\theta}^2 \right] \mathrm{d}s \tag{4}$$

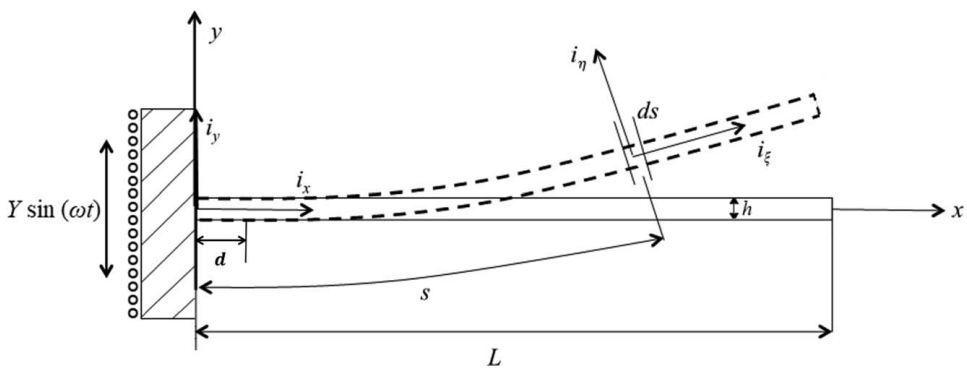


**Fig. 3 Beam flextural displacement with undeformed and deformed coordinate systems**

where the overdots denote the temporal partial derivatives. The strain energy due to flextural deformation is

$$U = \frac{1}{2}\int_0^L EI\rho^2 \mathrm{d}s \tag{5}$$

where $E$ and $I$ are the material elastic constant and second moment of inertia, respectively. The normalized flextural curvature associated with pure bending is $\rho$. The dissipated energy can be expressed as follows [24]:

$$W = \int_0^L f_d \,\mathrm{d}s = \int_0^L f_d \dot{v}\,\mathrm{d}t \tag{6}$$

The total damping force is [37]

$$f_d = c_1(1 + c_3 v^2)\dot{v} \tag{7}$$

The linear and nonlinear damping coefficients are $c_1$ and $c_3$, respectively.

To express the nonlinear displacement and its partial derivatives in convenient forms, Taylor series expansion is performed, where only terms up to the cubic order are kept. The axial displacement $u$ is expressed as a function of $v$ since $u$ and $v$ are small but finite [24]. The spatiotemporal energy equations are converted into manageable temporal forms through the application of the Rayleigh–Ritz method using assumed functions for the beam mode shapes [46]:

$$v(t, s) = \sum_{n=1}^{N} \Psi_n(s) q_n(t) \tag{8}$$

The generalized coordinate $q_n$ represents the time modulation of the $n$th mode expressed by an eigenfunction $\Psi_n$. Only the first flextural mode is considered since pure bending was the beam dominating mode in this study. The assumed function, Eq. (8), is then substituted into Eqs. (4), (5), and (6) to express the temporal forms of the kinetic, potential, and dissipation energies, respectively [24]:

$$T = \frac{1}{2}\left(m_s\int_0^L \Psi^2 \mathrm{d}s + I_r\int_0^L \Psi'^2 \mathrm{d}s\right)\dot{q}^2 + \frac{1}{2}\left[m_s\int_0^L\left(\int_0^\xi \Psi'^2 \mathrm{d}s\right)^2 \mathrm{d}s + I_r\int_0^L \Psi'^4 \mathrm{d}s\right]q^2\dot{q}^2 + \left(m_s\int_0^L \Psi \mathrm{d}s\right)\dot{Y}\dot{q} + \frac{1}{2}\left(m_s\int_0^L \mathrm{d}s\right)\dot{Y}^2 \tag{9a}$$

$$U = \frac{1}{2}\left(\int_0^L EI\Psi''^2 \mathrm{d}s\right)q^2 + \frac{1}{2}\left(\int_0^L EI\Psi''^2\Psi'^2 \mathrm{d}s\right)q^4 \tag{9b}$$

$$W = \frac{1}{2}\left[c_1\int_0^L \Psi^2 \mathrm{d}s + c_1c_3\left(\int_0^L \Psi^4 \mathrm{d}s\right)q^2\right]\dot{q}^2 \tag{9c}$$

Applying Lagrangian mechanics and normalized by the modal mass yield, the final equation of motion [24] is

$$\ddot{q} + m_3\left(q^2\ddot{q} + q\dot{q}^2\right) + \beta_{\mathrm{eq}}\dot{q} + k_{\mathrm{eq}}q = m_b\ddot{Y} \tag{10}$$

where the dynamic parameters are the

$$\text{nonlinear inertia:}\quad m_3 = m_s\int_0^L\left(\int_0^\xi \Psi'^2 \mathrm{d}s\right)^2 \mathrm{d}s + I_r\int_0^L \Psi'^4 \mathrm{d}s$$

$$\text{linear damping:}\quad \beta_l = c_1\int_0^L \Psi^2 \mathrm{d}s$$

$$\text{nonlinear damping:}\quad \beta_3 = c_1c_3\left(\int_0^L \Psi^4 \mathrm{d}s\right)$$

$$\text{linear stiffness:}\quad k_1 = \omega_n^2 = \int_0^d E_d I\Psi''^2 \mathrm{d}s + \int_d^L EI\Psi''^2 \mathrm{d}s$$

$$\text{nonlinear stiffness:}\quad k_3 = 2\left(\int_0^d E_d I\Psi''^2\Psi'^2 \mathrm{d}s\right) + 2\left(\int_d^L E_d I\Psi''^2\Psi'^2 \mathrm{d}s\right)$$

$$\text{driving inertial coefficient:}\quad m_b = -m_s\int_0^L \Psi \mathrm{d}s \tag{11}$$

Therefore,

$$\text{the equivalent damping is } \beta_{\mathrm{eq}} = \beta_1 + \beta_3 q^2 \text{ and equivalent stiffness is } k_{\mathrm{eq}} = k_1 + k_3 q^2 \tag{12}$$

**Table 1 Frequencies for modes I, II, and III obtained from the finite element method**

| | Mode I | Mode II | Mode III |
|---|---|---|---|
| Mode shape | Bend | Twist | Bend |
| Modal frequency (Hz) | 58.3 | 289 | 363 |
| Normalized modal frequency ($\omega_i/\omega_1$) | 1 | 4.96 | 6.23 |

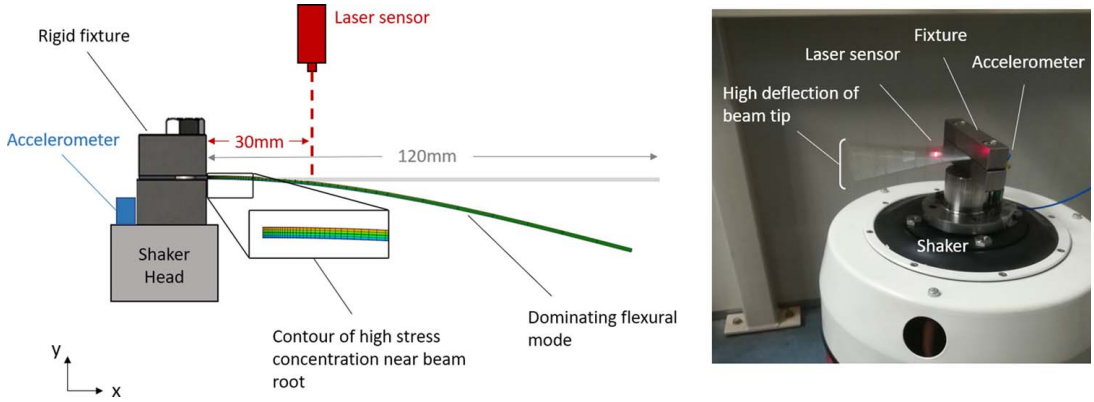


**Fig. 4 Vibration fatigue experiment showing high tip displacement of a beam**

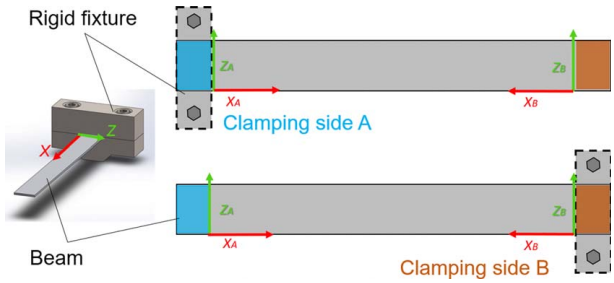


**Fig. 5 A and B configurations in blue and orange, respectively. Side A, beam was fatigue up to specified cycles. Beam was flipped to configuration B and fatigued to complete failure.**

where $d$ is the longitudinal distance of the material damaged region, starting from the clamped end of the beam (Fig. 3). During the early development of fatigue damage, it is reasonable to assume that the moment of inertia, $I$, will remain constant. As the damage buildups near the beam root, $k_1$ and $k_3$ are assumed to remain constant in the healthy section of the beam; i.e., $L-d$ region, in accordance to the fractional energy theory [7]. $E_d$ in a damaged region can be expressed as a function of the damage ratio, $D$, as follows [7]:

$$E_d = (1-D)E \tag{13}$$

To improve the model accuracy, $E_d$ is included in the stiffness coefficients to account for the spatially variation in material modulus due to damage accumulation.

The steady-state solution of the nonlinear ordinary differential equation (10) is obtained numerically using Matlab ODE solver, ODE45 function. The HBM is also utilized to perform algebraic calculation of the frequency response function (FRF), thus significantly reducing the computation time [34]. The harmonic trial solution is $q = A\sin(\omega t)$, with an amplitude, $A$. The excitation function in Eq. (10) can be expressed as $\bar{Y} = Y/m_b \sin(\omega t - \phi)$, where $Y$ is the excitation amplitude. Upon substituting the trial solution and excitation function in Eq. (10), the FRF becomes [34]

$$\frac{A^2}{Y^2} = \frac{1}{\left(k_{\text{eq}} - m_{\text{eq}}\omega^2\right)^2 + \beta_{\text{eq}}^2\omega^2} \tag{14}$$

where the equivalent stiffness is

$$k_{\text{eq}} = \omega_n^2 + \frac{3}{4}k_3A^2 \tag{15}$$

The equivalent mass and natural frequency are $m_{\text{eq}}$ and $\omega_n$, respectively. The backbone curve (Fig. 1) is

$$\omega_b^2 = \frac{k_{\text{eq}}}{m_{\text{eq}}} \pm \sqrt{-\frac{k_{\text{eq}}}{m_{\text{eq}}^3}} \tag{16}$$

Example of the backbone curve for nonlinear beam experiencing a dynamic hardening due to the geometric stiffness effect is shown in the figure.

## 3 Experimental Analysis

As stated previously, complete failure was defined as a 6 Hz net decrease in the structure resonance frequency, which turned out to be $\sim 1.2\times10^5$ cycles. The fatigue life was divided into three cases: 25%, 50%, and 75% of the total number of cycles to complete fatigue failure, i.e., each case consisted of $\sim 300\times10^3$ cycles. At the end of each fatigue case, the system identification steps shown in Fig. 2 were performed to extract the dynamic parameters and compare them to the beam baseline values. The experimental steps consisted of (i) free vibration, (ii) slow sine-sweep, and (iii) vibration fatigue.

**3.1 Experimental Setup.** The beam samples utilized in this study were aerospace-grade aluminum alloy, Al7075-T6. The material density and elastic modulus were approximately 2810 kg m$^{-3}$ and 71 GPa, respectively. The dimensions of each specimen were $150\times50\times1$ mm$^3$. The beam geometries were chosen to provide a generous separation between the first, $\omega_1$, and second, $\omega_2$, structural vibration modes to minimize potential modal coupling, where $\omega_2$ must be $\geq 3\omega_1$ [32]. In this study, $\omega_2 \cong 5\omega_1$, thus each beam was always under pure flextural displacement only. Table 1 reports the first three modal frequencies, which were obtained from finite element analysis using ABAQUS [30].

After clamping each beam sample to a rigid steel fixture, the system was attached to an electrodynamic shaker, as shown in Fig. 4. To maintain consistent boundary condition and uniform clamping pressure distribution, the fixture fasteners were torqued

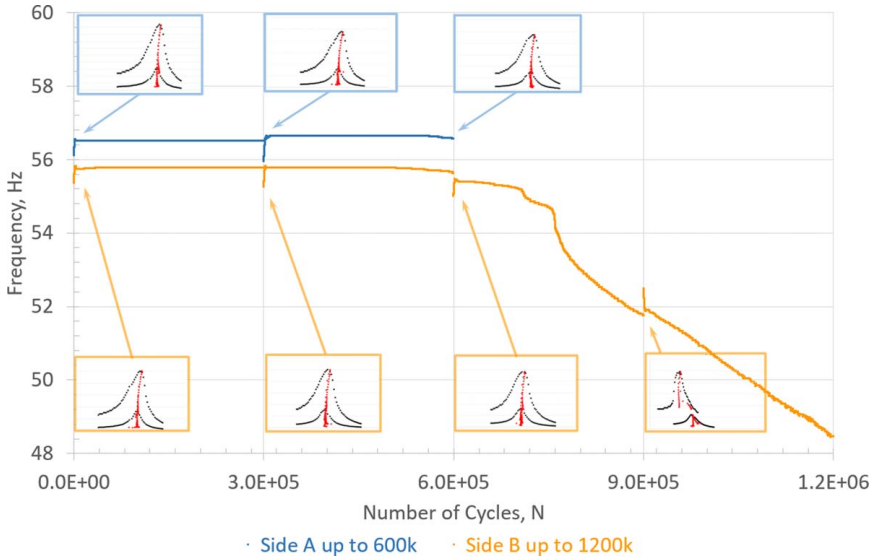


**Fig. 6 Frequency shift and changes in the response for each case as a function of fatigue cycles are shown in blue and orange dots for configurations A and B, respectively**

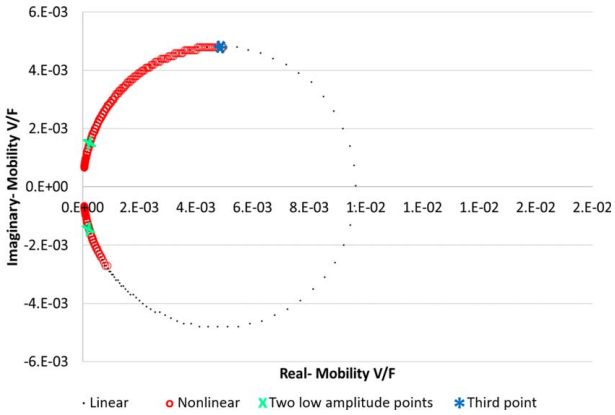


**Fig. 7 Nyquist plots for linear and nonlinear systems in black and red curves, respectively**

to 10 N m, and checked after completing each fatigue case. The base excitation provided by the shaker was controlled using an accelerometer sensor, PCB Piezotronics Model 333M0. The beam flextural displacement was measured at 30 mm from the clamped end using Polytec OFV-3001 laser vibrometer controller and OFV-303 sensor head (Fig. 4). The reason for locating the laser sensor at the 30 mm location from the fixture was to collect reliably velocity measurements within the laser sensor range limits. Moving the laser beam beyond the 30 mm distance will cause data clipping.

**3.2 Experimental Procedure.** To generate correlation between the materials degradation and changes in the dynamic parameters, each specimen was tested in two clamping configurations, A and B, as shown in Fig. 5 and highlighted in blue and orange, respectively. The clamping configuration of side A was performed for the 25%, 50%, and 75% fatigue cases. The beams were flipped to side B to perform fatigue testing until complete failure is reached. The example provided in Fig. 6 shows a beam in configuration A fatigued until $6 \times 10^5$ cycles were reached, then flipped to configuration B to fatigue until complete failure. Side A configuration allowed for performing material degradation analysis at 25% ($3 \times 10^5$ cycles), 50% ($6 \times 10^5$ cycles), and 75% ($9 \times 10^5$ cycles) prior to final fatigue. For side B, material characterization was performed only after complete failure.

The stepping frequency rate for both low and high amplitude sine-sweeps was set to 0.1 Hz. The linear and nonlinear parameters were calculated from the beam measured displacements for low and high amplitude sine-sweeps at 100 mV and 500 mV, respectively. Examples of the linear and nonlinear frequency response and backbone curves prior to vibration fatigue are shown in Fig. 6. Once a set of baseline parameters was established for an undamaged case, the vibration fatigue was performed every $3 \times 10^5$ cycles (Fig. 2).

The fatigue tests were carried out by setting the excitation frequency equal to the structural resonance obtained from the low amplitude sine-sweep tests. For all fatigue tests, the beam displacement amplitude was kept constant at 1.4 mm, which was measured by the laser sensor and controlled using proportional-integral-derivative. With fixed excitation frequency and response amplitude, the phase was traced, as detailed in Sec. 3.3. To ensure constant beam displacement, adjustments were made to the excitation frequency when the response phase exceeded a threshold limit, which was the beam resonance. Deviation from the threshold limit will require supplying the shaker with high electrical power and inducing high stresses on its components.

The example provided in Fig. 6 shows the frequency shift for configurations A and B. In Fig. 6 inset plots, the linear and nonlinear frequency response and backbone curves are shown in black and red marks, respectively. Clear distortions in the frequency response and backbone curves can be noticed when the fatigue exceeds $6 \times 10^5$ cycles, which is indicative of crack propagation. Additional details are provided in Sec. 4.

**3.3 Modified Carrella–Ewins Method.** Extracting the backbone curves can be achieved by using the Carrella–Ewins method [73]. Briefly, when applying the Carrella–Ewins method, the dynamic features are extracted by equating two receptance points at the same amplitude at either side of the FRF maximum peak. Therefore, the resonance and damping ratio can be calculated at that specific vibration response level. Subsequently, a discrete function describing the backbone and damping curves can be constructed by repeating this process from the lowest to highest response amplitudes. The shortfall of the Carrella–Ewins method, however, its assumption that both receptance branches are available, is not true for manifold points; notice the red curve in the

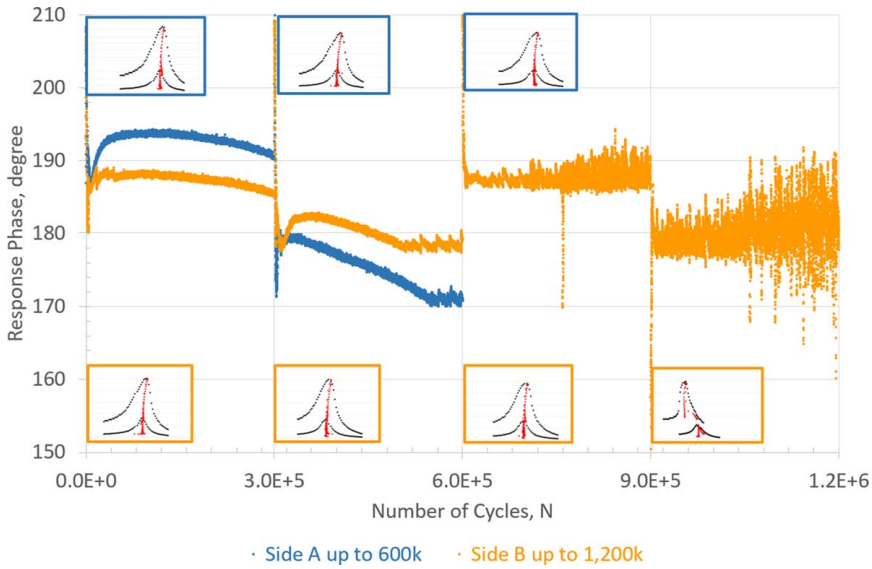


**Fig. 8 In situ phase trace versus fatigue cycles. Nonlinear response at the start and end of each fatigue case is shown for sides A and B in blue and orange colors, respectively.**

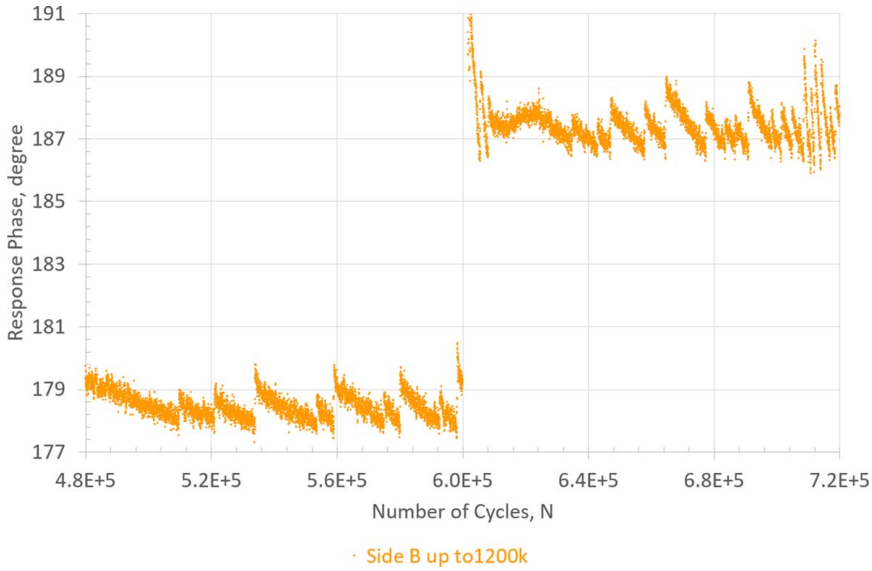


**Fig. 9 Segmented phase slopes due to updated excitation frequency; for configuration B**

Nyquist circle in Fig. 7. The Nyquist circles of the same dynamical system with its linear and nonlinear parameters are shown in black and red markers, respectively (Fig. 7). To overcome this limitation, our modified Carrella–Ewins method, instead, takes three mobility points (Fig. 7): two low amplitudes at either side of the FRF peak, shown in green markers, and a third point anywhere on the Nyquist plot, shown in a blue marker. Therefore, three is the minimum number of points for defining an FRF circle. The mobility points can be obtained as follows:

$$H(\omega)=\frac{i\omega}{(k-\omega^2 m)+i\omega c}=\frac{\omega^2 c}{(k-\omega^2 m)+\omega^2 c^2}+i\frac{\omega(k-\omega^2 m)}{(k-\omega^2 m)+\omega^2 c^2} \tag{17}$$

The three points are utilized to calculate the resonance frequency and linear damping. Keeping the same two low amplitudes points (nonlinearity is not active) and sweeping the third point, several triplets can be created each of which identifies a new linear Nyquist circle relative to the amplitude of the sweeping frequency point. Taking advantage of the Nyquist circularity, the linear damping is calculated from the diameter inverse. In Fig. 7, for example, two linear and nonlinear Nyquist circles are shown in black and red traces, respectively. When examining the linear response, it can be observed that every three frequency points obtained from the Nyquist data set always resolve the same circle. For linear response, all the frequency points are equally spaced within the circle's center. When the response is nonlinear, every three mobility points describe a new circle. Therefore, the Nyquist circle parameters are dependent on the magnitude of each selected point.

While there are several approaches for performing a circle fit or inverse FRF method, the Dobson approach was selected in this paper [74]. Briefly, the Dobson approach uses FRF points to build a series of straight lines each of which is curve-fitted. Both the angular coefficient and intercept are collected for each straight line to create two new straight lines. The Dobson approach is

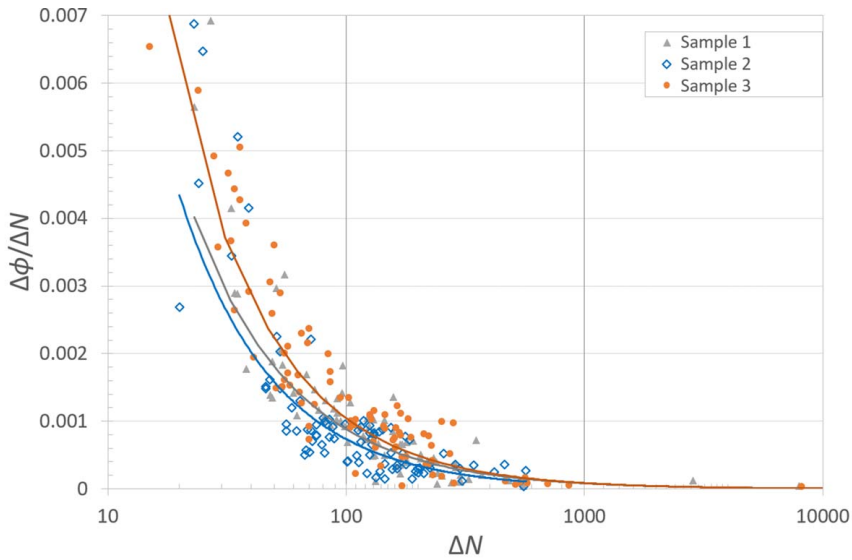


**Fig. 10 Example of the emerging segmented slopes in the phase traces as a function of fatigue cycles. The reported results are only for configuration B.**

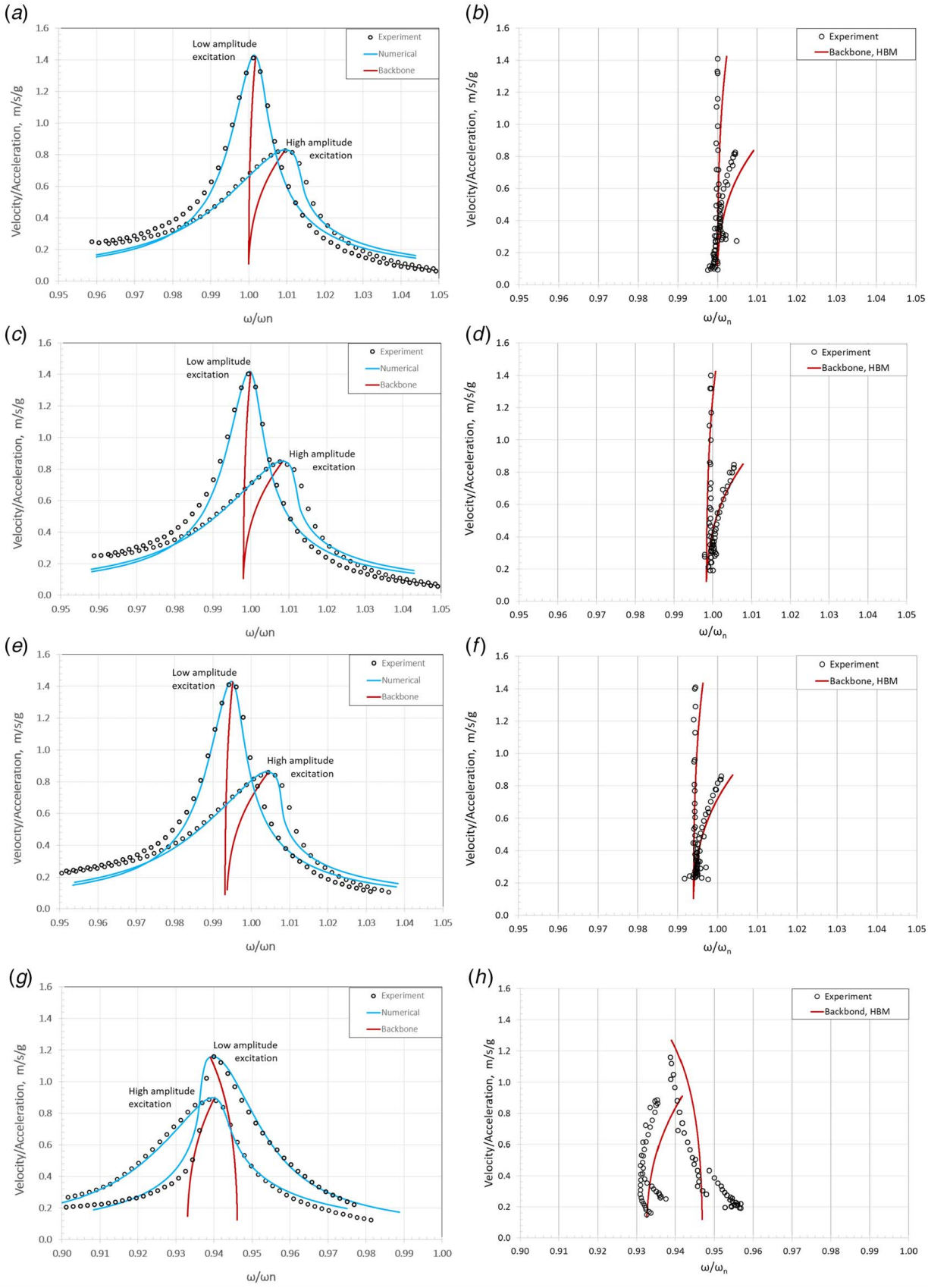


**Fig. 11 Evolution of the frequency response and backbone curves for 0, 300k, 600k, and 900k fatigue cycles. The analytical and experimental results are shown in solid lines and markers, respectively. (*a*) Response before fatiguing, (*b*) backbone before fatigue, (*c*) response after 300k cycles, (*d*) backbone after 300k cycles, (*e*) response after 600k cycles, (*f*) backbone after 600k cycles, (*g*) response after 900k cycles, and (*h*) backbone after 900k cycles.**

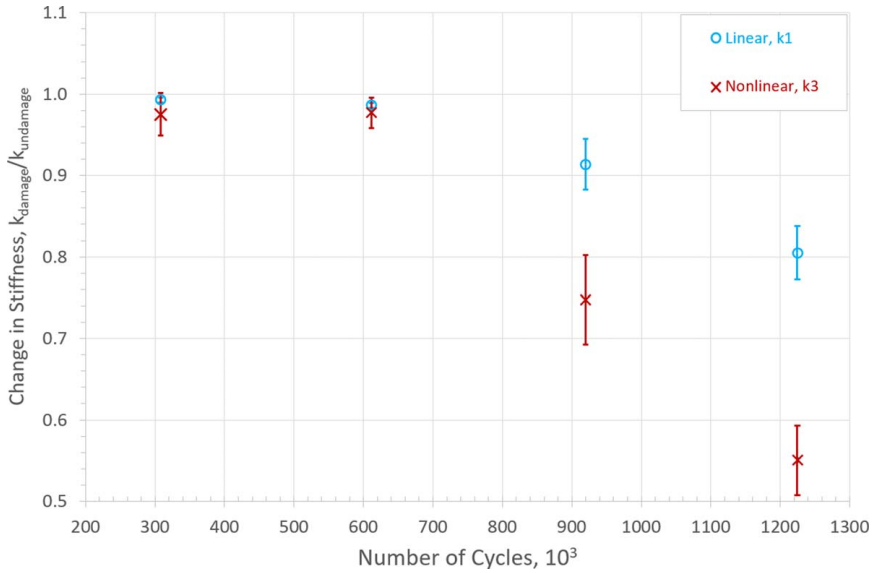


**Fig. 12 Evolution in the linear and nonlinear stiffness as a function of fatigue cycles**

extended to the Nyquist triplets to obtain the dynamic features. The frequency response and backbone curves for low and high amplitude of sine-sweeps calculated from the modified Carrella–Ewins method are reported as inset plots alongside the phase traces in Fig. 8. Additional examples are detailed in Sec. 4.2.

**3.4 Phase Tracking Method.** The phase was defined as the lag between the input force and response singles over the number of excitation cycles. The evolution in the phase was a more sensitive fatigue indicator than shift in the resonance (Fig. 8). Similar findings were reported for delamination onset in composites [75,76]. Utilizing the finite element method, Voudouris et al. showed that vibration response phase and delamination propagation were linearly correlated [77].

In this study, we borrow experimental strategy for composites reported in Refs. [75,76] to track the phase for aluminum samples exposed to vibration fatigue. In Fig. 9, the phase plotted as segmented slopes due to adjustments in the excitation frequency and details are provided in Sec. 3.2. For enhanced visualization of the response phase and its sensitivity to early fatigue damage, only phase traces between $4.8 \times 10^5$ and $7.2 \times 10^5$ cycles (Fig. 9).

## 4 Results and Discussion

This section is divided into two subsections. In Sec. 4.1, the main focus is on reporting and discussing the dynamic response of the tests samples before, during, and after exposure to high cycle fatigue. Both experimental and modeling results, in Sec. 4.1, consist of the FRF and backbone topology of pristine and fatigued cases. Analysis of in situ frequency and phase traces during fatigue testing is included. The comparison study between the experimental and analytical results are discussed in detail. Finally, Sec. 4.2 provides detailed insights into the evolution of the dynamic parameters as a function of fatigue cycles, as well as their sensitivity to material degradation over time.

**4.1 In Situ Identification Using the Phase Tracking Method.** It can be observed that the evolution trends in the phase traces for configurations A and B are similar (Fig. 8). This is an indication that flipping the beam from side A to B did not have any significant effect on the dynamic behavior of the beam. Overall, each phase trace is shown as a series of segmented lines plotted at their associated excitation frequencies, which were not updated until approximately $5 \times 10^5$ cycles.

While the emerging segmented phase slopes were indicative of early crack development, it was not clear why there was a slight jump in the phase between approximately $5 \times 10^5$ and $6 \times 10^5$ cycles, prior to updating the excitation frequency (Fig. 8). The phase increased after $6 \times 10^5$ cycles, followed by a drop after $9 \times 10^5$ cycles (Fig. 9). A potential explanation is the phase that appears to indicate material hardening followed by softening due to fatigue accumulation—a phenomenon reported in a previous study for Al 7075-T5 [47]. Insights into the relationship between the material hardening-softening phenomenon and phase shift is beyond the scope of this investigation and the subject of future studies.

Finally, calculating the phase change over the number of cycles $\Delta\phi/\Delta N$, described in Sec. 3.4, one can estimate the crack growth rate by means of phase evolution instead of the crack tip length. In Fig. 10, $\Delta\phi/\Delta N$ is reported for all three specimens, which illustrates the onset damage rate over the number of cycles. The rate of damage growth indicated by $\Delta\phi/\Delta N$ appears to be consistent for all three samples (Fig. 10), which means the method is repeatable. The data scatter was due to the manual collection of $\Delta\phi/\Delta N$. For the sake of completeness, crack growth in each specimen within each fatigue was verified, qualitative, using optical microscopy.

**4.2 Evolution in the Dynamic Parameters Due to Fatigue.** An example of the dynamic parameter identification for a beam experiencing fatigue is provided in Fig. 11, where the FRF and backbone curves are shown prior to fatigue testing, in Figs. 11(*a*) and 11(*b*), after $300 \times 10^3$ fatigue cycles in Figs. 11(*c*) and 11(*d*), $600 \times 10^3$ cycles in Figs. 11(*e*) and 11(*f*), and $900 \times 10^3$ cycles in Figs. 11(*g*) and 11(*h*), respectively. The experimental and modeling results are shown in markers and sold lines, respectively. The numerical solutions for the equation of motion, Eq. (10), and HBM, Eq. (16), are the blue and red curves, respectively, superimposed on top of the experimental results. The backbones were calculated from the experimental data using the modified Carrella–Ewins method, Eq. (17), and compared to the HBM (Figs. 11(*b*), 11(*d*), 11(*f*), and 11(*h*)). The amplitudes in Fig. 11 are reported as the maximum velocity normalized by the input acceleration.

The input frequencies were normalized by the natural frequency of the pristine specimens to show that the linear and nonlinear backbone curves overlapped with excellent agreements up to $600 \times 10^3$

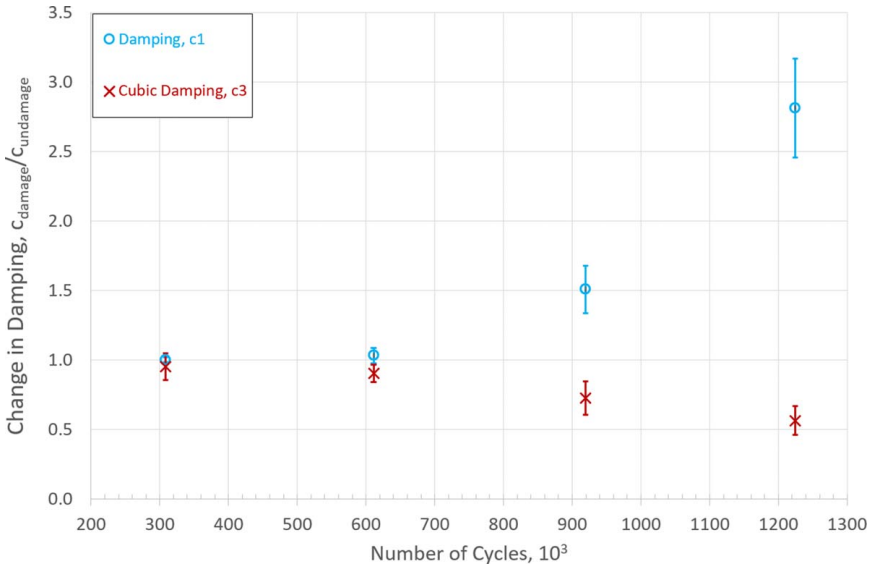


**Fig. 13 Evolution in the linear and nonlinear damping as a function of fatigue cycles**

cycles. Near $300 \times 10^3$ cycles, the fatigue damage led to distortion in the nonlinear response, where the maximum amplitude increased from approximately 0.82 m/s/g to 0.83 m/s/g (Fig. 11(*c*)). The insignificant drop in the natural frequency was approximately 0.2%. After completing $\sim 600 \times 10^3$ fatigue cycles, the FRF distortion remained unchanged, but the natural frequency dropped by approximately 0.8% (Figs. 11(*e*) and 11(*f*)). For the $900 \times 10^3$ cycles case, the linear FRF curve shows dynamic softening manifested by material compliance due to crack development [44,48]. At this point of the fatigue process, breathing-crack was developing [6].

The dynamic softening seen in the response signal was also captured analytically by updating the parameters $k_1$, $k_3$, $c_1$, and $c_3$, as discussed in Sec. 2. Using the sine-sweep tests, the linear stiffness, $k_1$, was calculated from the backbone curves. The decrease in $k_1$ as a function of cycles is shown in Fig. 12. The linear and nonlinear damping coefficients, $c_1$ and $c_3$, respectively, were obtained from the free-vibration experiments and reported in Fig. 13 as a function of fatigue cycles. After obtaining $k_1$, $c_1$, and $c_3$, the nonlinear geometric stiffness, $k_3$, in Eqs. (10) and (16) was to match the experimental results (Fig. 11).

Updating parameters $k_1$ and $k_3$ was achieved by adjusting the damage ratio, $D$, Eq. (13), up to $600 \times 10^3$ cycles. Due to the FRF distortion severity in the $900 \times 10^3$ cycle case, $D$ was adjusted only for $k_1$. However, $k_3$ was adjusted numerically to curve fit the linear and nonlinear FRFs. The decay in $k_1$ and $k_3$ parameters as a function of fatigue cycles is reported in Fig. 12. Both $k_1$ and $k_3$ were normalized by their respective initial values. Both $k_1$ and $k_3$ decreased logarithmically due to the increase in number of fatigue cycles. The logarithmic degradation in $k_3$, however, was more severe than that for $k_1$ after $600 \times 10^3$ cycles, which was consistent with fatigue studies by Andreaus and Casini [67] and Newman [78]. Figure 13 shows the beam displayed logarithmic decrease in $c_1$. However, $c_3$ increased exponentially as a function of fatigue cycles (Fig. 13). It is important to point out that the standard deviations of the calculated nonlinear parameters were higher than those for linear cases.

## 5 Conclusion

The paper illustrated that NSI holds promise as a viable tool for early fatigue damage diagnostics and monitoring. NSI was utilized for detecting and tracking fatigue in flexible aluminum structures exposed to vibratory loads. The nonlinear geometric stiffness, cubic damping, and phase shift were tracked as a function of fatigue cycles. Extracting the stiffness and damping coefficients required interrupting the fatigue tests. However, in situ phase tracing was accomplished successfully without interruptions using the proposed modified Carrella–Ewins method. The manifestation of material degradation due to fatigue accumulation can be identified from the (i) logarithmic decrease in the rate of change in phase and (ii) increase in the cubic damping accompanied with a decrease in the nonlinear geometric stiffness. It is important to point out that linear parameter identification was an inadequate technique in detecting early signs of fatigue.

Tracking the rate of changes in phase as a function of fatigue cycles appeared to be even more sensitive in detecting early signs of fatigue than any of the nonlinear parameters. Therefore, further studies are needed to gain deeper understanding of the physics required to exploit those parameters in a variety of materials and geometries to improve our capabilities for localizing, quantifying, and classifying early fatigue damage.

## Acknowledgment

We are grateful for ING. Z.A.J. Lok of Twente University for his assistant with the experimental design. We thank Drs. Daniel Cole and Todd Henry of the US Army Research Laboratory (ARL), Dr. Robert Haynes of U.S. Army DEVCOM Aviation & Missile Center for the helpful discussions. Ed Habtour gratefully acknowledges the support of Office of the Deputy Assistant Secretary of the U.S. Army for Defense Exports and Cooperation, and the Netherlands Organization for Applied Scientific Research under the Engineer and Scientist Exchange Program, as well as ARL Open Campus initiative.

## Conflict of Interest

There are no conflicts of interest.

## References

[1] Fasel, U., Keidel, D., Baumann, L., Cavolina, G., Eichenhofer, M., and Ermanni, P., 2020, "Composite Additive Manufacturing of Morphing Aerospace Structures," Manuf. Lett., **23**, pp. 85–88.
[2] Huang, J., Fu, X., and Jing, Z., 2021, "Singular Dynamics for Morphing Aircraft Switching on the Velocity Boundary," Commun. Nonlinear Sci. Numer. Simul., **95**, p. 105625.

[3] Henry, T. C., Johnson, T. E., Haynes, R. A., and Tran, A., 2021, "Fatigue Performance of Polyamide 12 Additively Manufactured Structures Designed With Topology Optimization," J. Test. Eval., **49**(3), pp. 1797–1813.

[4] Allen, J., and Ghoreyshi, M., 2018, "Forced Motions Design for Aerodynamic Identification and Modeling of a Generic Missile Configuration," Aerospace Sci. Technol., **77**, pp. 742–754.

[5] Noël, J. P., and Kerschen, G., 2017, "Nonlinear System Identification in Structural Dynamics: 10 More Years of Progress," Mech. Syst. Signal Process., **83**, pp. 2–35.

[6] Kharazan, M., Irani, S., and Reza Salimi, M., 2021, "Nonlinear Vibration Analysis of a Cantilever Beam With a Breathing Crack and Bilinear Behavior," J. Vib. Control, p. 10775463211018315.

[7] Habtour, E. M., Cole, D. P., Kube, C. M., Henry, T. C., Haynes, R. A., Gardea, F., Sano, T., and Tinga, T., 2019, "Structural State Awareness Through Integration of Global Dynamic and Local Material Behavior," J. Intell. Mater. Syst. Struct., **30**(9), pp. 1355–1365.

[8] Djeziri, M., Benmoussa, S., Mouchaweh, M. S., and Lughofer, E., 2020, "Fault Diagnosis and Prognosis Based on Physical Knowledge and Reliability Data: Application to MOS Field-Effect Transistor," Microelectron. Reliab., **110**, p. 113682.

[9] Gao, Z., and Liu, X., 2021, "An Overview on Fault Diagnosis, Prognosis and Resilient Control for Wind Turbine Systems," Processes, **9**(2), p. 300 .

[10] Farrar, C. R., and Worden, K., 2007, "An Introduction to Structural Health Monitoring," Philos. Trans. R. Soc. A: Math. Phys. Eng. Sci., **365**(1851), pp. 303–315.

[11] Lei, Y., Li, N., Guo, L., Li, N., Yan, T., and Lin, J., 2018, "Machinery Health Prognostics: A Systematic Review From Data Acquisition to RUL Prediction," Mech. Syst. Signal Process., **104**, pp. 799–834.

[12] Zhao, X. Y., Lang, Z.-Q., Park, G., Farrar, C. R., Todd, M. D., Mao, Z., and Worden, K., 2014, "A New Transmissibility Analysis Method for Detection and Location of Damage Via Nonlinear Features in MDOF Structural Systems," IEEE/ASME Trans. Mechatron., **20**(4), pp. 1933–1947.

[13] Wu, R.-T., and Jahanshahi, M. R., 2018, "Data Fusion Approaches for Structural Health Monitoring and System Identification: Past, Present, and Future," Struct. Health Monit., **19**(2), p. 1475921718798769.

[14] Moore, K. J., 2019, "Characteristic Nonlinear System Identification: A Data-Driven Approach for Local Nonlinear Attachments," Mech. Syst. Signal Process., **131**, pp. 335–347.

[15] Holford, K. M., Eaton, M. J., Hensman, J. J., Pullin, R., Evans, S. L., Dervilis, N., and Worden, K., 2017, "A New Methodology for Automating Acoustic Emission Detection of Metallic Fatigue Fractures in Highly Demanding Aerospace Environments: An Overview," Prog. Aerosp. Sci., **90**, pp. 1–11.

[16] Arslan, Ö., Aykan, M., and Nevzat Özgüven, H., 2011, "Parametric Identification of Structural Nonlinearities From Measured Frequency Response Data," Mech. Syst. Signal Process., **25**(4), pp. 1112–1125.

[17] Paulus, M., Dasgupta, A., and Habtour, E., 2012, "Life Estimation Model of a Cantilevered Beam Subjected to Complex Random Vibration," Fatigue Fract. Eng. Mater. Struct., **35**(11), pp. 1058–1070.

[18] Argaman, M., and Raveh, D. E., 2018, "Multioutput Autoregressive Aeroelastic System Identification and Flutter Prediction," J. Aircr., **56**(1), pp. 30–42.

[19] Liao, H., 2015, "Piecewise Constrained Optimization Harmonic Balance Method for Predicting the Limit Cycle Oscillations of an Airfoil with Various Nonlinear Structures," J. Fluids Struct., **55**, pp. 324–346.

[20] Montoya, A., Habtour, E., and Moreu, F., 2020, "Quantifying Information Without Entropy: Identifying Intermittent Disturbances in Dynamical Systems," Entropy, **22**(11), p. 1199.

[21] Shen, J., Su, Y., Liang, Q., and Zhu, X., 2018, "Calculation and Identification of the Aerodynamic Parameters for Small-Scaled Fixed-Wing UAVS," Sensors, **18**(1), p. 206.

[22] Egorov, A. G., Kamalutdinov, A. M., and Nuriev, A. N., 2018, "Evaluation of Aerodynamic Forces Acting on Oscillating Cantilever Beams Based on the Study of the Damped Flexural Vibration of Aluminium Test Samples," J. Sound Vib., **421**, pp. 334–347.

[23] Khodabakhshi, P., and Reddy, J. N., 2017, "A Unified Beam Theory With Strain Gradient Effect and the Von Kármán Nonlinearity," J. Appl. Math. Mech., **97**(1), pp. 70–91.

[24] Habtour, E., Cole, D. P., Stanton, S. C., Sridharan, R., and Dasgupta, A., 2016, "Damage Precursor Detection for Structures Subjected to Rotational Base Vibration," Int. J. Non-Linear Mech., **82**, pp. 49–58.

[25] Ostachowicz, W., and Krawczuk, M., 1991, "Analysis of the Effect of Cracks on the Natural Frequencies of a Cantilever Beam," J. Sound Vib., **150**(2), pp. 191–201.

[26] Hill, T. L., Cammarano, A., Neild, S. A., and Barton, D. A., 2017, "Identifying the Significance of Nonlinear Normal Modes," Proc. R. Soc. A: Math. Phys. Eng. Sci., **473**(2199), p. 20160789 .

[27] Shaw, A. D., Hill, T. L., Neild, S. A., and Friswell, M. I., 2016, "Periodic Responses of a Structure With 3:1 Internal Resonance," Mech. Syst. Signal Process., **81**, pp. 19–34.

[28] Tatar, M., and Masdari, M., 2019, "Investigation of Pitch Damping Derivatives for the Standard Dynamic Model at High Angles of Attack Using Neural Network," Aerospace Sci. Technol., **92**, pp. 685–695.

[29] Ooijevaar, T. H., Warnet, L. L., Loendersloot, R., Akkerman, R., and Tinga, T., 2016, "Impact Damage Identification in Composite Skin-Stiffener Structures Based on Modal Curvatures," Struct. Control Health Monit., **23**(2), pp. 198–217.

[30] Habtour, E., Paulus, M., and Dasgupta, A., 2014, "Modeling Approach for Predicting the Rate of Frequency Change of Notched Beam Exposed to Gaussian Random Excitation," Shock Vib., **2014** .

[31] Habtour, E., Connon, W. S., Pohland, M. F., Stanton, S. C., Paulus, M., and Dasgupta, A., 2014, "Review of Response and Damage of Linear and Nonlinear Systems Under Multiaxial Vibration," Shock Vib., **2014** .

[32] Ernst, M., Habtour, E., and Dasgupta, A., 2016, "Examining Steinberg's Octave Rule Applicability for Electronic Systems Exposed to Multiaxial Vibration," IEEE Trans. Components Pack. Manuf. Technol., **6**(4), pp. 561–568.

[33] Thomas, O., Sénéchal, A., and Deü, J.-F., 2016, "Hardening/Softening Behavior and Reduced Order Modeling of Nonlinear Vibrations of Rotating Cantilever Beams," Nonlinear Dyn., **86**(2), pp. 1293–1318.

[34] Akbarzade, M., and Farshidianfar, A., 2017, "Nonlinear Transversely Vibrating Beams by the Improved Energy Balance Method and the Global Residue Harmonic Balance Method," Appl. Math. Model., **45**, pp. 393–404.

[35] Butlin, T., Woodhouse, J., and Champneys, A., 2015, "The Landscape of Nonlinear Structural Dynamics: An Introduction," Phil. Trans. A Roy. Soc., A.373201404002014040O.

[36] Habtour, E., Sridharan, R., Dasgupta, A., Robeson, M., and Vantadori, S., 2018, "Phase Influence of Combined Rotational and Transverse Vibrations on the Structural Response," Mech. Syst. Signal Process., **100**, pp. 371–383.

[37] Li, D., and Shaw, S. W., 2020, "The Effects of Nonlinear Damping on Degenerate Parametric Amplification," Nonlinear Dyn., **102**(4), pp. 2433–2452.

[38] Di Sante, R., and Di Maio, D., 2020, "Corrigendum to "Measurement of Nonlinear Vibration Response in Aerospace Composite Blades Using Pulsed Airflow Excitation" [Measurement 130 (2018) 422–434] (Measurement (2018) 130 (422–434), (s0263224118307784), (10.1016/j. Measurement. 2018.08. 041))," Meas.: J. Int. Meas. Confederation, **160**, p. 107879.

[39] Cao, M. S., Sha, G. G., Gao, Y. F., and Ostachowicz, W., 2017, "Structural Damage Identification Using Damping: A Compendium of Uses and Features," Smart Mater. Struct., **26**(4), p. 043001.

[40] Ernst, M., Habtour, E., Dasgupta, A., Pohland, M., Robeson, M., and Paulus, M., 2015, "Comparison of Electronic Component Durability Under Uniaxial and Multiaxial Random Vibrations," J. Electron. Packag., **137**(1), p. 011009.

[41] Peele, B., Li, S., Larson, C., Cortell, J., Habtour, E., and Shepherd, R., 2019, "Untethered Stretchable Displays for Tactile Interaction," Soft Rob., **6**(1), pp. 142–149.

[42] Karličić, D., Cajić, M., and Adhikari, S., 2018, "Dynamic Stability of a Nonlinear Multiple-Nanobeam System," Nonlinear Dyn., **93**(3), pp. 1495–1517.

[43] Burt, P. M. S., and de Morais Goulart, J. H., 2018, "Efficient Computation of Bilinear Approximations and Volterra Models of Nonlinear Systems," IEEE Trans. Signal Process., **66**(3), pp. 804–816.

[44] Cole, D. P., Habtour, E. M., Sano, T., Fudger, S. J., Grendahl, S. M., and Dasgupta, A., 2017, "Local Mechanical Behavior of Steel Exposed to Nonlinear Harmonic Oscillation," Exp. Mech., **57**(7), pp. 1027–1035.

[45] Vantadori, S., Haynes, R., Fortese, G., Habtour, E., Ronchei, C., Scorza, D., and Zanichelli, A., 2018, "Methodology for Assessing Embryonic Cracks Development in Structures Under High-Cycle Multiaxial Random Vibrations," Fatigue Fract. Eng. Mater. Struct., **41**(1), pp. 20–28.

[46] Habtour, E., Cole, D. P., Riddick, J. C., Weiss, V., Robeson, M., Sridharan, R., and Dasgupta, A., 2016, "Detection of Fatigue Damage Precursor Using a Nonlinear Vibration Approach," Struct. Control Health Monit., **23**(12), pp. 1442–1463.

[47] Haynes, R. A., Habtour, E., Henry, T. C., Cole, D. P., Weiss, V., Kontsos, A., and Wisner, B., 2019, "Damage Precursor Indicator for Aluminum 7075-t6 Based on Nonlinear Dynamics," *Nonlinear Dynamics*, G. Kerschen, ed., Vol. 1, Springer, Orlando, FL, pp. 303–313.

[48] Henry, T., Cole, D., Kube, C., Fudger, S., Haynes, R., Mogonye, J., and Weiss, V., 2020, "Evaluation of Early Fatigue Signatures in Lightweight Aluminum Alloy 7075," Exp. Mech., **60**(2), pp. 205–216.

[49] Chakrapani, S. K., and Barnard, D. J., 2017, "Determination of Acoustic Nonlinearity Parameter ($\beta$) Using Nonlinear Resonance Ultrasound Spectroscopy: Theory and Experiment," J. Acoust. Soc. Am., **141**(2), pp. 919–928.

[50] Molla, M. H. U., Razzak, M. A., and Alam, M. S., 2016, "Harmonic Balance Method for Solving a Large-Amplitude Oscillation of a Conservative System With Inertia and Static Non-linearity," Results Phys., **6**, pp. 238–242.

[51] Chen, Y. M., and Liu, J. K., 2016, "A Precise Calculation of Bifurcation Points for Periodic Solution in Nonlinear Dynamical Systems," Appl. Math. Comput., **273**, pp. 1190–1195.

[52] Molnar, T. G., Insperger, T., and Stepan, G., 2019, "Closed-Form Estimations of the Bistable Region in Metal Cutting Via the Method of Averaging," Int. J. Non-Linear Mech., **112**, pp. 49–56.

[53] Cheng, C. M., Peng, Z. K., Zhang, W. M., and Meng, G., 2017, "Volterra-Series-Based Nonlinear System Modeling and Its Engineering Applications—A State-of-the-Art Review," Mech. Syst. Signal Process., **87**(2016), pp. 340–364.

[54] Hill, T. L., Neild, S. A., and Wagg, D. J., 2017, "Comparing the Direct Normal Form Method With Harmonic Balance and the Method of Multiple Scales," Proc. Eng., **199**, pp. 869–874.

[55] Lacarbonara, W., Carboni, B., and Quaranta, G., 2016, "Nonlinear Normal Modes for Damage Detection," Meccanica, **51**(11), pp. 2629–2645.

[56] Yan, Z., Taha, H. E., and Tan, T., 2017, "Nonlinear Characteristics of an Autoparametric Vibration System," J. Sound Vib., **390**, pp. 1–22.

[57] Jain, S., and Tiso, P., 2020, "Model Order Reduction for Temperature-Dependent Nonlinear Mechanical Systems: A Multiple Scales Approach," J. Sound Vib., **465**, p. 115022.

[58] Chakraborty, D., Kovvali, N., Papandreou-Suppappola, A., and Chattopadhyay, A., 2015, "An Adaptive Learning Damage Estimation Method for Structural Health Monitoring," J. Intell. Mater. Syst. Struct., **26**(2), pp. 125–143.

[59] Druce, J. M., Haupt, J. D., and Gonella, S., 2015, "Anomaly-Sensitive Dictionary Learning for Structural Diagnostics From Ultrasonic Wavefields," IEEE Trans. Ultrason. Ferroelectr. Freq. Control, **62**(7), pp. 1384–1396.
[60] Yang, J., Kang, G., Liu, Y., and Kan, Q., 2021, "A Novel Method of Multiaxial Fatigue Life Prediction Based on Deep Learning," Int. J. Fatigue, **151**, p. 106356.
[61] Zhang, Y., Hutchinson, P., Lieven, N. A., and Nunez-Yanez, J., 2020, "Remaining Useful Life Estimation Using Long Short-Term Memory Neural Networks and Deep Fusion," IEEE Access, **8**, p. 19 033.
[62] Koyuncu, A., Cigeroglu, E., and Özgüven, H., 2017, "Localization and Identification of Structural Nonlinearities Using Cascaded Optimization and Neural Networks," Mech. Syst. Signal Process., **95**, pp. 219–238.
[63] Brewick, P. T., Masri, S. F., Carboni, B., and Lacarbonara, W., 2017, "Enabling Reduced-Order Data-Driven Nonlinear Identification and Modeling Through Naïve Elastic Net Regularization," Int. J. Non-Linear Mech., **94**(February), pp. 46–58.
[64] Bosse, S., and Lechleiter, A., 2014, "Structural Health and Load Monitoring With Material-Embedded Sensor Networks and Self-Organizing Multi-Agent Systems," Procedia Technol., **15**, pp. 668–690.
[65] Rabiei, E., Droguett, E. L., and Modarres, M., 2018, "Fully Adaptive Particle Filtering Algorithm for Damage Diagnosis and Prognosis," Entropy, **20**(2), p. 100.
[66] Olivier, A., and Smyth, A. W., 2017, "Review of Nonlinear Filtering for SHM With an Exploration of Novel Higher-Order Kalman Filtering Algorithms for Uncertainty Quantification," J. Eng. Mech., **143**(11), p. 04017128.
[67] Andreaus, U., and Casini, P., 2016, "Identification of Multiple Open and Fatigue Cracks in Beam-Like Structures Using Wavelets on Deflection Signals," Continuum Mech. Thermodyn., **28**(1–2), pp. 361–378.
[68] Renson, L., Gonzalez-Buelga, A., Barton, D. A., and Neild, S. A., 2016, "Robust Identification of Backbone Curves Using Control-Based Continuation," J. Sound Vib., **367**, pp. 145–158.
[69] Xin, Y., Hao, H., and Li, J., 2019, "Time-Varying System Identification by Enhanced Empirical Wavelet Transform Based on Synchroextracting Transform," Eng. Struct., **196**, p. 109313.
[70] Londoño, J. M., Neild, S. A., and Cooper, J. E., 2015, "Identification of Backbone Curves of Nonlinear Systems From Resonance Decay Responses," J. Sound Vib., **348**, p. 224–238.
[71] Londoño, J. M., Cooper, J. E., and Neild, S. A., 2017, "Identification of Systems Containing Nonlinear Stiffnesses Using Backbone Curves," Mech. Syst. Signal Process., **84**, pp. 116–135.
[72] Lu, Z. Q., Hu, G. S., Ding, H., and Chen, L. Q., 2018, "Jump-Based Estimation for Nonlinear Stiffness and Damping Parameters," JVC/J. Vib. Control, **25**(2), pp. 325–335.
[73] Carrella, A., and Ewins, D., 2011, "Identifying and Quantifying Structural Nonlinearities in Engineering Applications From Measured Frequency Response Functions," Mech. Syst. Signal Process., **25**(3), pp. 1011–1027.
[74] Dobson, B., 1987, "A Straight-Line Technique for Extracting Modal Properties From Frequency Response Data," Mech. Syst. Signal Process., **1**(1), pp. 29–40.
[75] Magi, F., Di Maio, D., and Sever, I., 2016, "Damage Initiation and Structural Degradation Through Resonance Vibration: Application to Composite Laminates in Fatigue," Compos. Sci. Technol., **132**, pp. 47–56.
[76] Magi, F., Di Maio, D., and Sever, I., 2017, "Validation of Initial Crack Propagation Under Vibration Fatigue by Finite Element Analysis," Int. J. Fatigue, **104**, pp. 183–194.
[77] Voudouris, G., Di Maio, D., and Sever, I. A., 2020, "Experimental Fatigue Behaviour of CFRP Composites Under Vibration and Thermal Loading," Int. J. Fatigue, **140**, p. 105791.
[78] Newman, J., 2015, "Fatigue and Crack-Growth Analyses Under Giga-Cycle Loading on Aluminum Alloys," Procedia Eng., **101**, pp. 339–346.